J Mater Sci (2009) 44:2925–2930
DOI 10.1007/s10853-009-3386-y

Microstructural characterization of nanocrystalline nickel produced by surface mechanical attrition treatment

Wei Li · Ping Liu · Fengcang Ma · Yonghua Rong

Received: 16 January 2009 / Accepted: 4 March 2009 / Published online: 25 March 2009

Abstract By means of surface mechanical attrition treatment (SMAT), nanocrystalline surface layers are produced in pure Ni plates. The average crystallite size, root mean square (r.m.s.) microstrain, dislocation density, and stored elastic energy are determined by X-ray diffraction (XRD) line profile analysis. The average crystallite size obtained by XRD is compared with the grain size observed from transmission electron microscopy (TEM) image. The high-resolution TEM (HRTEM) micrograph confirms the presence of high density of dislocations obtained by XRD, and reveals that most of dislocations distribute at the subgrain boundaries with few inside the subgrains.

Introduction

Severe plastic deformation (SPD), as an effective method of producing bulk nanocrystalline materials by imposing intense plastic strains into metallic materials, has attracted the growing interests of specialists [1]. Nanocrystalline materials processed by SPD have unusual and extraordinary mechanical and physical properties that are different from and often superior to those of their conventional coarse-grained counterparts. Many techniques based on SPD, such as equal channel angular pressing (ECAP) [2], high pressure torsion (HPT) [3], accumulative roll-bonding (ARB) [4], have been developed and used to process bulk nanocrystalline materials extensively.

As an alternative to SPD, surface mechanical attrition treatment (SMAT), is recently developed to produce bulk nanocrystalline surface layer with the gradient distribution of grain sizes along the depth [5]. The basic principle of SMAT is the generation of plastic deformation in the surface layer of a bulk material by means of the repeated multidirectional impact of the hardened steel balls. The plastic deformation under the high strain rate results in a progressive refinement of coarse grains into a nanometer scale in the surface layer. It has been succeeded in achieving surface nanocrystallization of a variety of materials including pure metals and alloys [6–9].

Pure Ni represents a useful model material for the investigation of processing by SPD [10]. Several authors have investigated the microstructures of Ni samples processed by ECAP [10, 11], HPT [12], and their combinations [13]. However, the microstructure of nanocrystalline Ni produced by SMAT has seldom been reported. The primary objective of the present investigation is to study the microstructure of the SMATed nanocrystalline Ni by using X-ray diffraction (XRD), transmission electron microscopy (TEM) and high-resolution TEM (HRTEM). Particular attention is paid to the dislocation distribution in the nanocrystalline grains.

Experimental

Three plates (80 × 80 × 8 mm^3) of pure Ni (≥99.96 wt%) were annealed at 973 K for 60 min and water-quenched to obtain the homogeneous coarse grains, and then suffered from SMAT. The SMAT set-up and processing have been described in details elsewhere [8]. In brief, the hardened

W. Li (✉) · P. Liu · F. Ma
School of Mechanical Engineering, University of Shanghai for Science and Technology, Shanghai 200093, China
e-mail: liwei176@usst.edu.cn

W. Li · Y. Rong
School of Materials Science and Engineering, Shanghai Jiao Tong University, Shanghai 200240, China

steel balls were placed at the bottom of a cylinder-shaped vacuum chamber attached to a vibration generator. Because of the high vibration frequency of the system, the sample surface was struck repetitively by a large number of balls, resulting in a progressive refinement of coarse grains into the nanometer scale. In this work, the plates were treated for 30, 60, and 90 min, respectively at a vibrating frequency of 50 Hz with the hardened steel balls with 8 mm in diameter.

Small samples ($10 \times 10 \times 0.3$ mm^3) were obtained by electric spark cutting the surface layer, and then were studied by XRD peak profile analysis. The diffraction profiles were measured by a D/max-2550 X-ray diffractometer (18 kW) with Cu K_α radiation. The step size and step time were 0.02° and 5 s, respectively. The instrumental correction was made by using the powder pattern of a Si standard and Stokes correction procedure [14]. The selected reflection of Ni, 111, was evaluated for the average crystallite size, root mean square (r.m.s.) microstrain, dislocation density, and stored elastic energy by the modified Warren–Averbach method described in Sect. Evaluation of the X-ray diffraction line profiles.

The microstructure was characterized by JEM-100CX TEM at 100 kV and JEM-2100F HRTEM at 200 kV. The TEM foils were prepared by mechanical polishing from the untreated side and finally thinned by argon ion milling.

Evaluation of the X-ray diffraction line profiles

Based on the Warren–Averbach Fourier method [15] which provides the apparent crystallite size and the mean square strain, Wilkens [16] proposed a model of "restrictedly random" distribution of dislocations to analyze the line profiles and the dislocations density $\overline{\rho}$, configuration parameter $\overline{M}$, strain field range $\overline{R_e}$, stored elastic energy E/V could be deduced for monocrystal copper. Considering the idea suggested by Langford [17] that each profile could be regarded as a convolution of several Gaussian functions with Cauchy ones, Wang et al. [18, 19] worked out a practical procedure and standard curves for line profile analysis of face-centered cubic (fcc), body-centered cubic (bcc), and hexagonally close packed (hcp) polycrystals. However, two orders of reflections are needed in this method, which makes it unavailable for the case when it can only observe the high-quality first-order reflection, such as nanocrystalline Ni processed by SMAT. As a result, the combination of single-peak Fourier analysis proposed by Mignot and Rondot [20] and Wang et al's method [18, 19] is used in the present work. The fitting procedures are given as follows.

By Stokes' deconvolution of XRD profile, the physical broadened profiles and its corresponding Fourier coefficients $A(L)$ are obtained, and then the two components, "particle" coefficients $A^{\mathrm{p}}(L)$ and "strain" coefficients $A^{\mathrm{s}}(L)$, are separated as

$$A^{\mathrm{p}}(L) = a - \frac{L}{D} \tag{1}$$

$$A^{\mathrm{s}}(L) = \exp\left(\frac{-2\pi m^2 L^2 \left\langle \varepsilon_L^2 \right\rangle}{d^2}\right) \tag{2}$$

where a is the quantity expressing the "hook" effect, L the specific length perpendicular to the reflecting planes, D the average coherent domain size, m the order of reflection, $\left\langle \varepsilon_L^2 \right\rangle^{1/2}$ the r.m.s. microstrain, d the interplanar spacing of the reflection plane. Combining with the method proposed by Mignot and Rondot [20], D and $\left\langle \varepsilon_L^2 \right\rangle^{1/2}$ can be obtained by non-linear fitting.

According to Wang's theory [18], "strain" coefficients $A^{\mathrm{s}}(L)$ can be expressed as

$$A^{\mathrm{s}}(L) = \exp\left(-2\beta_{\mathrm{c}} L - \pi \beta_{\mathrm{g}}^2 L^2\right) \tag{3}$$

where β_{c} and β_{g} are the Cauchy and Gaussian widths of "strain" broadened profile, which can be gained from Eq. 1 and 3 by non-linear fitting. Making use of the standard curves and procedures described in [19], the average dislocation density $\overline{\rho}$ and configuration parameter $\overline{M}$ can been obtained and they directly give the stored elastic energy E/V:

$$\frac{E}{V} = AG\overline{\rho}b^2 \ln\frac{\overline{M}}{r_0\sqrt{\overline{\rho}}} \tag{4}$$

where $A = 1/4\pi$ for screw dislocations, $A = 1/4\pi(1-\nu)$ for edge dislocations, ν is Poisson's ratio, G the shear modulus, b Burgers vector length, and r_0 dislocation core radius. In the calculation of the stored elastic energy, the proportions of the screw dislocation and edge dislocation are assumed to be equal.

Results and discussion

Figure 1a shows the typical microstructure of the water-quenched Ni sample after being annealed at 973 K for 60 min. The grains are almost equiaxed and the average grain size is about 10–40 μm. Figure 1b indicates a cross-sectional SEM observation of the Ni sample after SMAT for 60 min. Obviously, microstructure morphology of the treated layer differs from that in the matrix. The original coarse grains in the surface layer are severely refined into ultrafine grains, in which grain boundaries could not be identified. The microstructures in the treated layer change gradually from ultrafine-grained structures in the topmost layer to the undeformed and polygonal grains in the matrix. The whole thickness of the deformed layer is about 50 μm.

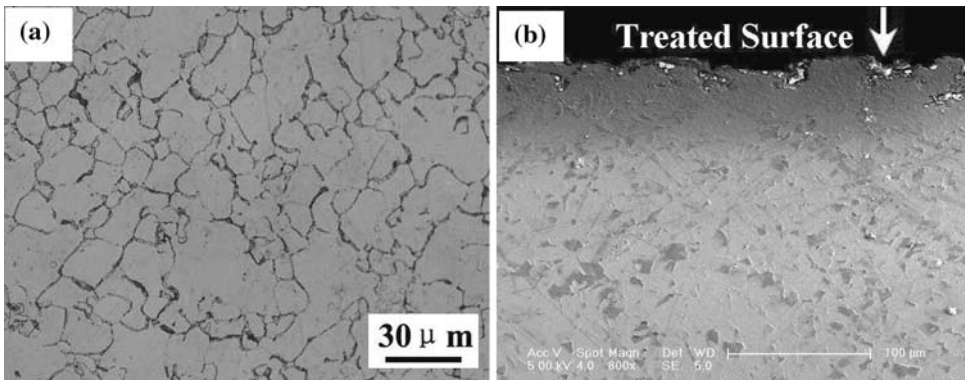

Fig. 1 Microstructure of Ni **a** held at 973 K for 60 min following water-quenched and **b** after SMAT for 60 min

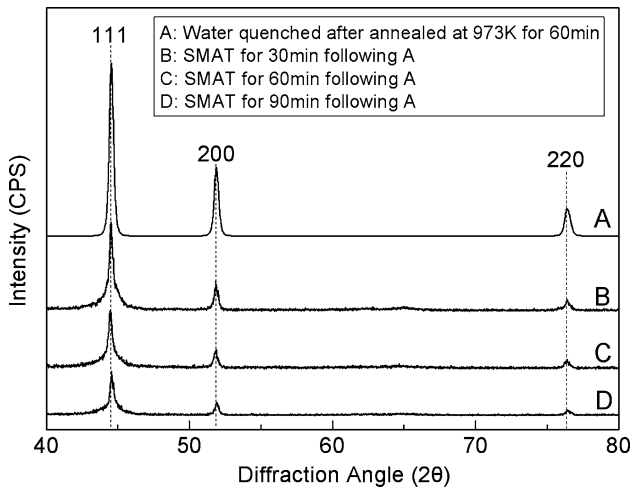

Fig. 2 XRD profiles of the surface layers in Ni before and after SMAT

Figure 2 shows the XRD profiles of the surface layers in the water-quenched and SMATed 30, 60, and 90 min Ni samples. It is clear that the water-quenched and SMATed samples all consists of only fcc phase, showing no formation of new phase during SMAT process. It is clearly seen that there exists a significant broadening of Bragg reflections in the SMATed samples comparing with the water-quenched one, which can be attributed to the grain refinement and the presence of a high level of microstrain. The 111 reflection was selected to evaluate the microstructural parameters, including the average crystallite size (D), r.m.s. microstrain ($\langle \varepsilon_L^2 \rangle^{1/2}$), average dislocation density ($\overline{\rho}$), and stored elastic energy E/V, using the modified Warren–Averbach method in Sect. Evaluation of the X-ray diffraction line profiles. It should be noted that, although different parameters can be obtained from different reflections related to texture component, it is valid to compare with the parameters obtained from same reflection. The results are shown in Table 1, in which the errors come from the fitting calculations using ORIGIN software.

From Table 1, it can be seen that the value of D for the water-quenched sample is about 472 nm and the order of magnitude of $\overline{\rho}$ is as low as 10^{13} m^{-2}. With increasing SMAT time, the D values drop into nanometer scale rapidly. After 60 min SMAT, the value of D reaches about 9 nm and the value of $\langle \varepsilon_L^2 \rangle^{1/2}$ rises to as high as about 10 times of that in the water-quenched state. The values of $\overline{\rho}$ and E/V after 60 min SMAT are about 7.6×10^{15} m^{-2} and 2.5×10^7 J/m^3, respectively, which are both two order of magnitude larger than those in the water-quenched sample, indicating that strongly developed defect structure exists in the SMATed samples. Such high value of dislocation density was also found in nanocrystalline materials prepared by other SPD methods [13, 21].

Figure 3 indicates the TEM micrographs of the topmost layer in the Ni sample after SMAT for 60 min. The bright-field image of Fig. 3a shows that the sample consists of nanocrystalline grains. The dark-field image of Fig. 3b clearly indicates that the nanocrystalline grains are roughly equiaxed and the average grain size is about 8 nm, which is consistent with the XRD result (9 ± 2 nm).

Generally, the crystallite size of SPD-processed nanocrystalline materials determined by XRD is smaller than

Table 1 Microstructural parameters of Ni under different SMAT times

SMAT time (min)	(hkl)	D (nm)	$\langle \varepsilon_L^2 \rangle^{1/2} \times 10^{-3}$	$\overline{\rho}$ (m^{-2})	E/V (Jm^{-3})
Water-quenched state	111	472 ± 24	0.5 ± 0.1	(5.5 ± 0.4) × 10^{13}	(2.5 ± 0.2) × 10^5
30	111	12 ± 3	4.4 ± 0.3	(5.8 ± 0.5) × 10^{15}	(2.1 ± 0.2) × 10^7
60	111	9 ± 2	5.5 ± 0.4	(7.6 ± 0.7) × 10^{15}	(2.5 ± 0.2) × 10^7
90	111	7 ± 2	6.8 ± 0.5	(11.1 ± 0.9) × 10^{15}	(3.6 ± 0.3) × 10^7

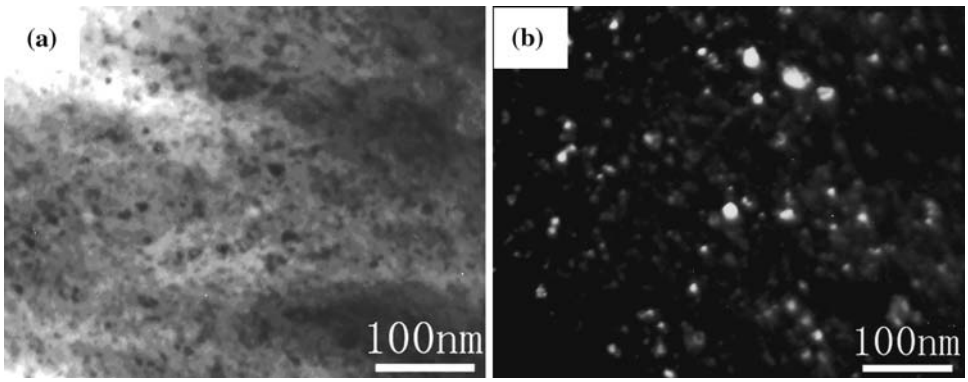

Fig. 3 TEM images of topmost surface layer in Ni after SMAT for 60 min **a** bright-field **b** dark-field image

that by TEM [22]. During SPD process, the dislocations formed in the grain interiors can arrange into dislocation cell boundaries to minimize their strain-energy [23]. As a result, subgrains will form inside the original grains, separated by low angle grain boundary with small misorientations. XRD is able to distinguish these subgrains with small misorientations [22], even less than 1°–2°, and therefore, gives the average size of dislocation cells or subgrains, while the conventional TEM dark-field image provides the size of the grains featured by high angle grain boundary. In other words, a grain displayed in conventional TEM micrograph may consist of several subgrains recognized by XRD, which is verified by HRTEM image in Fig. 4.

Figure 4a shows the typical nanocrystalline grain presented in the conventional TEM image with the size of about 20 nm. From the magnified image in Fig. 4b, it can be seen that this nanocrystalline grain consists of several subgrains, which are marked by A, B, C, D, respectively. These subgrains are separated by low angle grain boundary with small misorientations. XRD can identify the different subgrains and therefore, gives the average size of subgrains, that is, less than 10 nm. In contrast, the conventional TEM image can only provides the size of the whole grain (about 20 nm). Therefore, the average crystallite size obtained by XRD should be remarkably smaller that by TEM. However, as mentioned above, the two measured sizes are in good agreement with each other in the present work. This can be attributed to the gradient distribution of grain sizes along the deformed depth of the SMATed sample and the different measuring depths of XRD and TEM. TEM observation comes from the information of the topmost surface layer of less than 0.5 μm thick, while XRD results average the information of a surface layer of about 5 μm thick [24]. With the increase of the deformed depth, the grain size increases. As a result, the average crystallite size measured by XRD is inclined to approach to the grain size observed from TEM image.

Figure 5 is a Fourier filtered HRTEM micrograph of Fig. 4b, which shows a large number of dislocations and heavy distortion of lattice. By counting the number of dislocations within this area, the dislocation density was estimated as about 4.0×10^{16} m^{-2}. This measurement is only qualitative but not quantitative and therefore, is different from the result in Table 1. However, it confirms the presence of the high density of dislocations in the SMATed nanocrystalline Ni. In order to investigate the dislocation distribution in the nanocrystalline grain, the subgrain labels

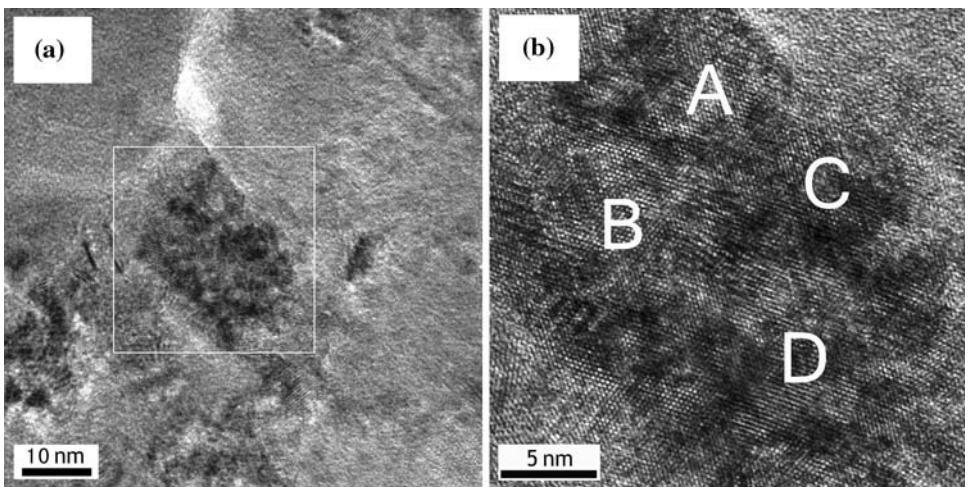

Fig. 4 **a** HRTEM micrograph of a nanocrystalline grain in Ni after SMAT for 60 min and **b** magnified image from the white frame

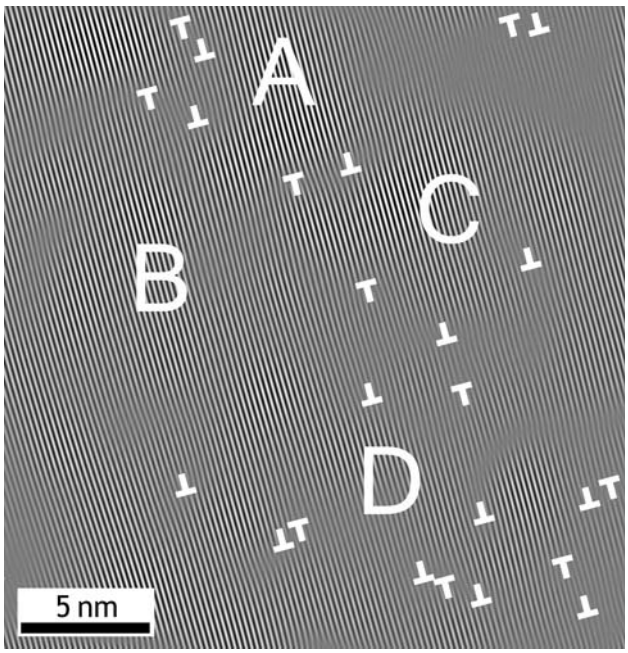

Fig. 5 Fourier filtered micrograph of the image in Fig. 4b

of A, B, C, D are also marked in Fig. 5 at the same positions in the Fig. 4b. It can be seen that a majority of dislocations distribute at subgrain and grain boundaries, while few dislocations locate in the subgrain interior. The similar phenomenon was also observed in other nanocrystalline materials processed by SPD [25, 26]. When the grain size reduces to the nanometer scale, especially less than a critical size, the dislocations are not intensively stored in grain interiors but absorbed by the grain boundaries [27]. The excessive dislocations exist at grain boundary region, which makes grain boundary be in high-energy and non-equilibrium state.

The formation of such distribution is due to the nanocrystallization mechanism of Ni. Lu et al. [28] suggested that the nanocrystallization process was related with the stacking fault energy (SFE) of metallic materials. Ni is a typical fcc metal with a medium SFE value (about 125 mJ/m^2 [29]). The nanocrystallization process should include the development of equiaxed dislocation cells, formation of twins and subgrain boundaries with small misorientations, and evolution of subgrain boundaries to highly misoriented grain boundaries. During the SMAT process, the dislocation activities lead to formation of dislocation cells where high density of dislocations locates at the cell boundary. With further treatment, dislocation cells can transform into the subgrain grains with small misorientation, in which high density of dislocations locate at the subgrain boundaries with few dislocations inside the subgrains, as shown in Fig. 5. At this time, the thickness of the subgrain boundaries is comparatively large, about 3–5 nm based on Fig. 5. As the SMAT process proceeds, the thickness of the subgrain boundaries will decrease and the misorientations between the neighboring subgrains will increase through the grain boundary sliding and grain rotation [30, 31], till the subgrain boundaries are transformed into the conventional grain boundaries with large misorientations.

Conclusions

The nanocrystalline surface layers are produced in Ni samples by SMAT for different times. The average crystallite size, r.m.s. microstrain, dislocation density, and stored elastic energy are evaluated from XRD profiles by the modified Warren–Averbach method. The results indicate that the average crystallite size drops rapidly into the nanometer scale with the increase of SMAT time, and high values of r.m.s. microstrain, dislocation density, and stored elastic energy are obtained as SMAT proceeds. After SMAT for 60 min, the average crystallite size, dislocation density, and stored elastic energy are 9 ± 2 nm, $(7.6 \pm 0.7) \times 10^{15}$ m^{-2} and $(2.5 \pm 0.2) \times 10^7$ J/m^3, respectively. The HRTEM micrograph confirms the presence of high density of dislocations obtained from XRD, and reveals that most of dislocations distribute at the subgrain boundaries with few dislocations inside the subgrains.

Acknowledgement The present work was financially supported by the National Natural Science Foundation of China under Grant No. 50871069.

References

1. Valiev RZ, Islamgaliev RK, Alexandrov IV (2000) Prog Mater Sci 45:103. doi:10.1016/S0079-6425(99)00007-9
2. Zhao YH, Liao XZ, Jin Z, Valiev RZ, Zhu YT (2004) Acta Mater 52:4589. doi:10.1016/j.actamat.2004.06.017
3. Xu C, Horita Z, Langdon TG (2008) J Mater Sci 43:7286. doi:10.1007/s10853-008-2624-z
4. Saito Y, Utsunomiya H, Tsuji N, Sakai T (1999) Acta Mater 47:579. doi:10.1016/S1359-6454(98)00365-6
5. Lu K, Lu J (1999) J Mater Sci Technol 15:193
6. Zhang HW, Hei ZK, Liu G, Lu J, Lu K (2003) Acta Mater 51:1871. doi:10.1016/S1359-6454(02)00594-3
7. Tao NR, Wang ZB, Tong WP, Sui ML, Lu J, Lu K (2002) Acta Mater 50:4603. doi:10.1016/S1359-6454(02)00310-5
8. Wang K, Tao NR, Liu G, Lu J, Lu K (2006) Acta Mater 54:5281. doi:10.1016/j.actamat.2006.07.013
9. Wen CS, Chen Z, Huang BX, Rong YH (2006) Metall Mater Trans A 37:1413. doi:10.1007/s11661-006-0086-y
10. Neishi K, Horita Z, Langdon TG (2002) Mater Sci Eng A 325:54. doi:10.1016/S0921-5093(01)01404-6
11. Zhilyaev AP, Nurislamova GV, Baro MD, Valiev RZ, Langdon TG (2002) Metall Mater Trans A 33:1865. doi:10.1007/s11661-002-0197-z
12. Zhilyaev AP, Lee S, Nurislamova GV, Valiev RZ, Langdon TG (2001) Scripta Mater 44:2753. doi:10.1016/S1359-6462(01)00955-1

13. Zhilyaev AP, Gubicza J, Nurislamova GV, Revesz A, Surinach S, Baro MD, Ungar T (2003) Phys Status Solidi A 198:263. doi:10.1002/pssa.200306608
14. Stokes AR (1948) Proc Phys Soc 61:382. doi:10.1088/0959-5309/61/4/311
15. Warren BE, Averbach BL (1950) J Appl Phys 21:595. doi:10.1063/1.1699713
16. Wilkens M (1970) Phys Status Solidi A 2:359. doi:10.1002/pssa.19700020224
17. Langford JI (1978) J Appl Cryst 11:10. doi:10.1107/S0021889878012601
18. Wang YM, Lee SS, Lee YC (1982) J Appl Cryst 15:35. doi:10.1107/S0021889882011315
19. Zwui S, Chen G, Wang YM (1985) J Mater Sci Lett 4:1434. doi:10.1007/BF00721356
20. Mignot J, Rondot D (1977) Acta Cryst A 33:327. doi:10.1107/S0567739477000795
21. Ungar T (2007) J Mater Sci 42:1584. doi:10.1007/s10853-006-0696-1
22. Ungar T, Tichy G, Gubicza J, Hellmig RJ (2005) Powder Diffr 20:366. doi:10.1154/1.2135313
23. Hughes DA, Hansen N (2000) Acta Mater 48:2985. doi:10.1016/S1359-6454(00)00082-3
24. Li W, Wang XD, Meng QP, Rong YH (2008) Scripta Mater 59:344. doi:10.1016/j.scriptamat.2008.04.001
25. Zhu YT, Huang JY, Gubicza J, Ungar T, Ma E, Valiev RZ (2003) J Mater Res 18:1908. doi:10.1557/JMR.2003.0267
26. Li W, Xu WZ, Wang XD, Rong YH (2009) J Alloys Compd 474:546. doi:10.1016/j.jallcom.2008.06.136
27. Baretzky B, Baro MD, Grabovetskaya GP, Gubicza J et al (2005) Rev Adv Mater Sci 9:45
28. Lu K, Lu J (2004) Mater Sci Eng A 375–377:38. doi:10.1016/j.msea.2003.10.261
29. Carter CB, Holmes SM (1977) Philos Mag 35:1161. doi:10.1080/14786437708232942
30. Shan Z, Stach EA, Wiezorek JMK, Knapp JA, Follstaedt DM, Mao SX (2004) Science 305:654. doi:10.1126/science.1098741
31. Zhu YT, Langdon TG (2005) Mater Sci Eng A 409:234. doi:10.1016/j.msea.2005.05.111